Acta Mechanica Sinica (2013) 29(5):682–698
DOI 10.1007/s10409-013-0070-x

RESEARCH PAPER

# A micromechanical model for effective conductivity in granular electrode structures

**Julia Ott · Benjamin Völker · Yixiang Gan · Robert M. McMeeking · Marc Kamlah**

Received: 4 July 2013 / Accepted: 6 August 2013


**Abstract** Optimization of composition and microstructure is important to enhance performance of solid oxide fuel cells (SOFC) and lithium-ion batteries (LIB). For this, the porous electrode structures of both SOFC and LIB are modeled as a binary mixture of electronic and ionic conducting particles to estimate effective transport properties. Particle packings of 10 000 spherical, binary sized and randomly positioned particles are created numerically and densified considering the different manufacturing processes in SOFC and LIB: the sintering of SOFC electrodes is approximated geometrically, whereas the calendering process and volume change due to intercalation in LIB are modeled physically by a discrete element approach. A combination of a tracking algorithm and a resistor network approach is developed to predict the connectivity and effective conductivity for the various densified structures. For SOFC, a systematic study of the influence of morphology on connectivity and conductivity is performed on a large number of assemblies with different compositions and particle size ratios between 1 and 10. In comparison to percolation theory, an enlarged percolation area is found, especially for large size ratios. It is shown that in contrast to former studies the percolation threshold correlates to varying coordination numbers. The effective conductivity shows not only an increase with volume fraction as expected but also with size ratio. For LIB, a general increase of conductivity during the intercalation process was observed in correlation with increasing contact forces. The positive influence of calendering on the percolation threshold and the effective conductivity of carbon black is shown. The anisotropy caused by the calendering process does not influence the carbon black phase.

**Keywords** Granular electrode structures · Effective conductivity · Percolation

J. Ott (✉) · M. Kamlah
Institute of Applied Materials,
Karlsruhe Institute of Technology,
76131 Karlsruhe, Germany
e-mail: julia.ott@kit.edu

B. Völker · R.M. McMeeking
Department of Mechanical Engineering,
University of California,
Santa Barbara, CA 93106, USA

Y. Gan
School of Civil Engineering, The University of Sydney,
NSW 2006, Australia

R.M. McMeeking
Materials Department, University of California,
Santa Barbara, CA 93106, USA
School of Engineering, University of Aberdeen,
King's College, Aberdeen, AB24 3UE, Scotland, UK
INM - Leibniz Institute for New Materials,
Campus D2 2, 66123 Saarbrücken, Germany

**Nomenclature**

| | |
|---|---|
| $c_0$ | initial $Li^+$ concentration |
| $c_x$ | momentary $Li^+$ concentration |
| $c_{\max}$ | maximum $Li^+$ concentration |
| $D$ | diffusivity |
| $f_n$ | normal force |
| $f_t$ | tangential force |
| $I$ | flux respectively current |
| $\boldsymbol{K}$ | conductivity matrix |
| $k_{\text{bulk},l}$ | conductivity of bulk material |
| $k_{\text{eff},l}$ | effective conductivity of granular structure |
| $L$ | box length |
| $\boldsymbol{n}_i$ | normal unit vector |
| $P_l$ | percolation probability |
| $PF$ | packing factor |
| $R$ | resistance between 2 particles |
| $R_{\max}$ | resistance of a cylinder with $r_p$ and $\delta$ |
| $r_0$ | initial particle radius |
| $r_c$ | contact radius |
| $r_x$ | momentary particle radius |

| | |
|---|---|
| $T$ | temperature |
| $t$ | time |
| $\boldsymbol{t}_j$ | tangential unit vector |
| $u$ | displacement |
| $V$ | voltage |
| $x_i$ | position of particle $i$ |
| $Z_0$ | overall coordination number |
| $Z_{l,l}$ | number of contacts of a $l$-particle to other $l$-particles |

**Greek symbols**

| | |
|---|---|
| $\delta$ | distance between two particles |
| $\epsilon$ | porosity |
| $\varepsilon$ | strain |
| $\nu$ | Poisson's ratio |
| $\sigma$ | stress |
| $\phi_l$ | volume fraction |
| $\varphi$ | potential |
| $\Omega$ | partial molar volume |

**Subscripts**

| | |
|---|---|
| AM | active material |
| bulk | bulk property |
| CB | carbon black |
| eff | effective property |
| $i$ | particle label |
| $l$ | species |
| max | maximum |
| SP | small particles |
| $x$ | momentary state |
| 0 | initial state |

## 1 Introduction

Solid oxide fuel cells (SOFC) and lithium-ion batteries (LIB) are attractive solutions for clean energy conversion and storage. In order to make them competitive to conventional solutions, efficiency and durability need to be improved further.

Composition and microstructure of electrodes in chemical power sources in general play a critical role for high electrode performance of the cells, as shown e.g. in Ref. [1] for LIB or in Refs. [2, 3] for SOFC. The electrodes in consideration are a mixture of ion conducting and electron conducting particles forming a porous composition to sustain the transport of electrons, ions and further reactants to and from the active sites, where the energy releasing reaction takes place. Since the electrochemical processes within the cells are strongly coupled, a change in one morphological parameter, e.g. particle size ratio or volume fraction, influences all transport properties and, as a consequence the overall cell performance. Hence, for optimization it is crucial not only to understand how effective transport properties improve cell performance but also which morphology provides the required characteristics. In this work we focus on the second part and present an approach to determine the influence of morphological parameters on the individual effective transport properties.

We consider the granular, porous electrode structure as a binary mixture of spherical particles. In SOFC anodes yttria-stabilized zirconia (YSZ) and nickel (Ni) are the most common materials; LIB electrodes contain carbon black (CB) to enhance electric conductivity and active material (AM). Due to the similarities in the electrode structures described, the same modeling approaches are applied here to investigate microstructural influences on the effective conductivity.

SOFC cells are nowadays mostly manufactured from monomodal powders. As suggested in Ref. [3], larger size ratios and volume fractions adjusted for the size ratio can lead to an improvement in cell power if at the same time connectivity of both phases is sustained. To find an optimized cell design it is important to understand the influence of variation in microstructure on percolation probability and the overall transport properties.

$Li_xMn_2O_4$ or $Li_xFePO_4$ are promising electrode materials for LIB in terms of costs, high theoretical capacity and stability; however, low electric conductivity limits the field of application. To overcome this, CB is added to enhance the conductivity [1]. Connectivity to the current collector and active material is required to affect the effective electron conductivity and must be maintained during loading and unloading of the cell. As the intercalation processes of $Li^+$ in the active material lead to volume changes and therefore internal stresses, rearrangements in the granular electrode structure are possible. This can lead to changes in connectivity and conductivity. To our knowledge this has not been considered in most approaches for modeling the effective conductivity in LIB.

For the determination of effective conductivity $k_{\text{eff}}$ in porous composite materials exist numerous models. The most simple methods are based on the solid volume fraction $\phi_l$ of the phase $l$ and porosity $\epsilon$ only, such as the Bruggeman approach, which can be reduced to $k_{\text{eff},l} = k_{\text{bulk},l}[(1-\epsilon)\phi_l]^{1.5}$ if only the phase $l$ is conducting; or Maxwell theory, which is valid for low amount of inclusions only [4]. These theories are mostly developed for specific applications and may not be applicable for any arbitrary microstructure. And as the probability of finding percolating paths through the microstructure is not considered in the Bruggeman equation or similar approaches [5], they are not applicable to investigate connectivity. Connectivity however, is required in SOFC for both phases and in LIB for the CB phase.

Therefore, as an additional feature the Bruggeman equation is enhanced by a term for the percolation probability. This describes the probability of a connecting pathway of one phase $l$ through a binary mixture. It is estimated based on a critical volume fraction where the transition from non-percolating to percolating takes place. Bouvard [6] found the percolation threshold to correlate to a specific coordination number $Z_{l,l}$ of 2 for arbitrary binary powder mixtures even though the critical volume fraction varies for different size ratios. Here, the coordination number $Z_{l,l}$ describes the number of contacts a particle of species $l$ has to particles of the same species. It is determined analytically from the

the size ratios and volume fractions of an arbitrary binary mixture as shown in Ref. [2] considering an overall coordination number $Z_0$ of 6. Thus, the effective conductivity of the species $l$ can be estimated with an adjusted Bruggeman equation under consideration of the percolation probability $P_l$ of the phase $l$

$$k_{\text{eff},l} = k_{\text{bulk},l}[(1-\epsilon)\phi_l P_l]^{1.5}. \quad (1)$$

Based on percolation theory, investigations of the influence of particle size and volume fraction on conductivity and in general cell performance have been performed [2, 3, 7], showing a clear dependency of percolation and conductivity on size ratio and volume fraction. But as the basic correlations where found for undensified, binary powders with size ratios below 3, this theory may not hold true for larger size ratios or densified structures. Porosity, coordination number or percolation threshold used in percolation theory may differ from the values in the densified electrode structures and therefore should be reexamined carefully. Furthermore, it is not known if the correlations can be applied for changes in microstructure caused by mechanical loading as happens in LIB.

To overcome the shortcomings of the volume averaging theories, cell performance was directly calculated on discretized microstructures, which are either determined by focus ion beam-scanning electron microscope (FIB-SEM) tomography [8] or numerically generated [9]. FIB-SEM tomography is the most accurate approach to describe the microstructure, however it is only applicable for yet existing microstructures and moreover very costly. Therefore it does not allow for a systematic investigation of the influence of morphological parameters on the effective transport properties. Besides, it provides only a snapshot of the electrode structure and consequently the approach is incapable of tracking microstructural changes.

Although numerically generated microstructures are only an approximation of reality, they enable the systematic investigation of certain parameters such as size ratio, volume fraction etc. separately. A number of researchers have simulated either cubic lattices with randomly assigned species to each site (e.g. [10]) or randomly distributed particles (e.g. [9]). Different approaches have been used to determine the effective conductivity of these structures. The most straightforward way is to discretize the structure and solve the differential transport equations on the mesh with commercial FE solutions [11]. In comparison to other approaches this is quite expensive in terms of computational power required. Another method working on discretized structures is the lattice Monte–Carlo (LMC) approach, which determines diffusivity from the mean displacement of a large number of random walkers [12]. Hence, it is intrinsically a computationally demanding method as well. A third method is to convert the particulate structure directly into a resistor network and solve Kirchhoff's law. Most such approaches aim for solving the electrochemical processes directly on the microstructure. However, in Ref. [13] it has been discussed that some of the ongoing electrochemical processes such as gas-phase diffusion in SOFC are best treated on a continuum basis instead of a network method. We propose to employ the resistor network method focused on the calculation of the effective conductivities alone. This is done for each phase in numerical generated microstructures to obtain more valid input data for a more precise phenomenological continuum cell model. In this way, we also gain knowledge of the influence of microstructural changes, either due to varying compositions or rearrangements during loading, to the transport properties of a single phase of the system.

The objective of this work is to develop a tool which allows for calculation of the effective conductivities of each phase in binary, granular mixtures. This will be used to investigate the influence of changes in microstructure on effective conductivity. As a systematic study of a multitude of microstructures will be performed, a fast and flexible method is required. Therefore, we choose the resistor network approach. With the results gained here, future calculations with, for example, Dual–Foil model in LIB [14] and porous electrode theory in SOFC [2, 3] can be more accurate in terms of morphology and allow for more reliable statements regarding microstructural optimization.

The paper is organized as follows: Sect. 2 the numerical generation of microstructures is explained, then the methods for calculating effective conductivity are introduced in Sect. 3. For validation some exemplary calculations are conducted and results are compared with averaging methods and the well established lattice Monte–Carlo method in Sect. 4. Concluding, results for various electrode compositions in SOFC as well as for microstructural rearrangements during intercalation processes in LIB will be shown and discussed.

## 2 Porous electrode structures

For the generation of random close packed microstructures exist several algorithms, which can be divided in algorithms using sequential addition of particles [15] and algorithms starting from a random distribution of points [15–18]. In contrast to the later, the first group of methods leads to rather low densities and, in addition, do not allow for periodic boundary conditions in all three directions. As only periodic boundaries allow for modeling bulk material, the later methods are more suitable for this work. Among the later, the one suggested by Jodrey and Tory [15] allows for controlling the packing factor ($PF$) by a single parameter and has therefore been adjusted by Gan [19] for binary sized packings. This adjusted algorithm is used in our work. Additionally to $PF$, this method allows to define number of particles $N$, particle size ratio, solid volume fractions $\phi_l$ in advance. The packing factor is controlled by a single parameter as described in Ref. [15]. First, the center coordinates of the $N$ spherical particles are distributed randomly in into a box of a given size $L_x \times L_y \times L_z$ (often a cube with $L_x = L_y = L_z$). The particles are associated with two radii: an outer radius $\tilde{r}_{\text{out}}$

which is initially set to yield a nominal packing factor of 100% and an inner radius $\tilde{r}_{\text{in}}$ defined by the worst overlap of the assembly. For monosized assemblies all particle radii correspond directly to the calculated values, whereas for binary packings the individual particle radii are scaled by a factor $f(I)$ in dependence of the size ratio. This results for a particle $I$ in $r^I_{\text{out}} = f(I)\tilde{r}_{\text{out}}$ and $r^I_{\text{in}} = f(I)\tilde{r}_{\text{in}}$. To generate a microstructure from this initial configuration two steps are carried out iteratively. First, the worst overlap is reduced by moving the two particles apart. This leads mostly to a smaller overlap and therefore a larger inner radius. As a second step the outer radii are reduced depending on the prescribed contraction rate. The iteration process stops, when the difference between outer and inner radius is smaller than the tolerance. With the implementation of periodic boundary conditions (PBCs), the assemblies represent bulk regions inside the electrodes. An exemplary microstructure with a particle size ratio of 10 and a solid volume fraction of 15% of small particles is shown in Fig. 1. This procedure leads to microstructures which in an ideal case just contain one contact. Therefore, the structures need to be densified further to generate a more realistic electrode structure.

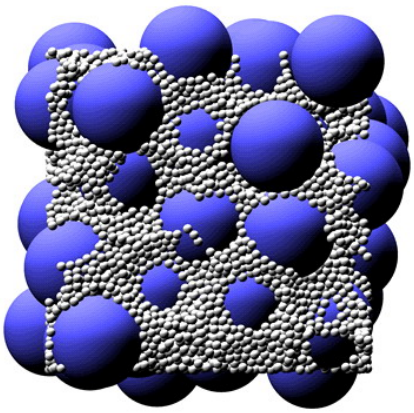

**Fig. 1** Numerically generated periodic porous electrode structure with a particle size ratio of 10 and solid volume fraction of 15% of small particles. All particles of one phase have the same size

For SOFC electrode structures, the randomly generated microstructure is further densified by a procedure of numerical sintering. Schneider et al. [9] use a diffusion based discrete element model to determine the electrode structure. As there are many unknown quantities in sintering and reduction during cell processing, the numerically generated structure is densified purely geometrically by increasing the radii to a certain amount while the particle centers are kept fixed. According to Ref. [20] an electrode porosity $PF_{\text{exp}}$ of around 74% is measured for monosized powders, whereas the numerically generated structures with monosized spheres have a packing factor $PF_{\text{num}}$ of 64%. The amount of densification is determined from the ratio of these values as $PF_{\text{exp}}/PF_{\text{num}} = 1.16$. As described, SOFC electrodes are considered in this work as a mixture of ionic and electronic conducting phases. The most common materials for the anode are YSZ as ion conducting phase and Ni as electron conducting phase. Therefore in the further course of this work the ion conducting particles of SOFC are referred to as YSZ and the electron conducting phase as Ni, even so the results are applicable for other choice of materials. For the systematic investigation of SOFC electrode structures a multitude of assemblies is generated with size ratios YSZ to Ni from 1 to 10 and solid volume fractions Ni between 0 and 1. For each composition 10 assemblies are made for statistical purpose. All microstructures are densified by the same amount. This leads to packing factors between 74% for monosized and 86% solid fraction for large size ratios.

In LIB the effective conductivity is not only influenced by composition but also by mechanical effects due to the volume change of active material (AM) during $Li^+$ intercalation. For example in $Li_xMn_2O_4$ the volume increases up to 6% [21], in silicon electrodes a volume increase of up to 300% was observed [22]. Carbon black has usually a size of about 40nm. As for high rate applications the particle size of active material is proposed to be in the range of several 100 nm [1], we choose a radius ratio of 10 for AM to CB. For the determination of the percolation threshold of CB we look at different compositions in the range of 10% to 15% solid volume fraction of CB (Volume $\text{frac}_{\text{CB}}$). Experiments show that initial porosities of 30% to 40% solid volume fraction lead to good cell performance [23]. Therefore, the structures are generated with either low (L) or high (H) packing factor of 67.3% or 69.4% solid volume fraction, respectively. For purposes of statistical evaluation, we generated three assemblies per data point. The average values are listed in Table 1.

**Table 1** Composition of the samples

| No | Volume $\text{frac}_{\text{CB}}$/% | $PF_{\text{ini}}$ low (L)/% | $PF_{\text{ini}}$ high (H)/% |
|---|---|---|---|
| 1 | 10 | 67.33 ± 0.08 | 69.43 ± 0.05 |
| 2 | 12.5 | 67.29 ± 0.07 | 69.43 ± 0.08 |
| 3 | 15 | 67.31 ± 0.09 | 69.47 ± 0.08 |

To investigate the impact of microstructural changes due to intercalation on effective conductivity, discrete element modeling (DEM) is used to densify the microstructure. In DEM each particle is treated as a discrete object, interacting mechanically with its neighbors through its contacts. As the particles are assumed to be elastic, a Hertz–Mindlin type contact law is applied to calculate the contact forces acting on each particle. Newton's law is applied to calculate acceleration, velocity and new position of the particles iteratively until mechanical equilibrium is reached. Details about the DEM simulations can be found in Ref. [24] . The material parameters used in the DEM calculations are given in Table 2.

The intercalation process is modeled by gradually increasing the radius $r_x$ of the AM linearly with the $Li^+$ concentration. This is calculated in analogy to thermal expan-

sion as

$$\frac{r_x - r_0}{r_0} = \frac{\Omega}{3}(c_x - c_0) \tag{2}$$

with $r_0$ as initial particle radius, $(c_x - c_0)$ as change in $Li^+$ concentration and $\Omega$ as partial molar volume, which was calculated in accordance to Zhang et al. [25]. The 6% volume increase of $Li_xMn_2O_4$ is equivalent to a radius increase of 2%.

**Table 2** Material parameters for the DEM simulation

| Parameter | Value |
|---|---|
| Young's modulus $E_{AM}$/GPa | 25 [26] |
| Young's modulus $E_{CB}$/GPa | 6 [26] |
| Poission's ratio $\nu$ | 0.3 [25] |
| Volume increase | 6% [21] |
| Partial molar volume $\Omega$/(mol·m$^{-3}$) | $2.62 \times 10^{-6}$ |
| Maximum $Li^+$ concentration $c_{max}$/(mol·m$^{-3}$) | $2.29 \times 10^4$ [25] |
| Uni-axial strain $\varepsilon_{xx}$ | 0.02 |

Additionally, the assemblies with high packing factor are also densified with a combined process of calendering and intercalation to investigate the influence of calendering on the effective conductivity of the electrode structure. In this work the calendering of the assemblies is modeled as uni-axial compression. A strain $\varepsilon_{ij}$ of 2% in total is applied gradually by moving each particle $i$ at the beginning of each loading step by

$$\Delta x_j = \Delta \varepsilon_{ij} x_i \tag{3}$$

with $x_i$ as the position of the particle center. Then, the compressed microstructure is further densified by the previously described intercalation process.

## 3 Modeling effective conductivity in granular materials

Several steps have to be performed to determine the effective conductivity of the generated microstructures.

### 3.1 Percolation probability

Within a binary mixture of two components with bulk conductivities differing by several orders of magnitude, the effective conductivity is closely related to percolation: if the amount of one component is too low to constitute a connecting cluster through a certain volume, this component does not contribute to the assembly's conductivity. Percolation probability describes the likelihood that particles form such a connecting cluster through the electrode. Isotropic percolation means that all boundaries are connected by one cluster. Directional percolation is given if there is a connecting cluster from one side of the box to the opposite side in each direction $(x, y, z)$ separately. For investigation of possible anisotropic characteristics, we look for percolation in each direction separately.

To determine the connectivity the Hoshen–Kopelman algorithm (HK) introduced by Refs. [27, 28] has been implemented in C++ and extended to account for PBC. The algorithm was originally developed for lattice structures [29]. Its single and sequential pass through the lattice (Fig. 2) linearizes the time and memory space requirement as a function of the lattice size: it passes through the structure only once and assigns each occupied site (blue in Fig. 2) to a cluster. If two yet existing clusters are found to be connected, this information is stored separately in a vector of much smaller size and the clusters are relabeled after the run through the lattice is completed.

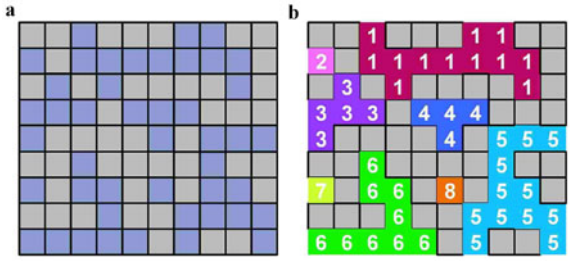


**Fig. 2** **a** Lattice with randomly assigned occupation (dark) to each site; **b** Cluster found with Hoshen–Kopelman algorithm considering the sites as connected if they share an edge

For illustration purpose only, the extension of the lattice through periodic boundaries is explained in the following on a lattice structure even though it was only implemented for non-lattice structures. The periodic boundary conditions can lead to additional connectivity as shown in Fig. 3 for cluster 1. First, periodic boundaries are generated by copying the already labeled original lattice structure in all directions (Fig. 3a). This leads to a state where lattice sites belonging originally to cluster 1 are in direct contact with cluster 5 or 6 and vice versa. Clearly these particles also belong to the clusters they are directly connected to. This leads to a combined cluster 1 containing the former cluster 5 and 6 (Fig. 3b). Cluster 1 now connects the opposite edges horizontally. Based on this, we define unidirectional percolation as a state in which a cluster contains original sites on one side of the lattice and the periodic copies of these sites on the opposite side of the lattice as shown in Fig. 3c. This is done for all three directions separately. For adapting this to a non-lattice approach the binary mixtures are separated into the two phases. They are transformed in random graphs containing information on particle location (nodes) and contact information (links). The nodes are randomly numbered consecutively and the algorithm runs through this array of numbers sequentially, assigning each node to a certain cluster. After each particle within the assembly and within the periodic boundaries is assigned to a certain cluster, the clusters connected through PBCs are merged, as explained previously. The percolation probability is calculated from the ratio of percolated particles of one species to the overall num-

ber of this species within the assembly [6].

When a phase of a structure is found to be percolating, conductivity can be calculated considering just those particles belonging to the percolated clusters. To transform this cluster into an electrical network, the resistance between two contacting particles has to be calculated.

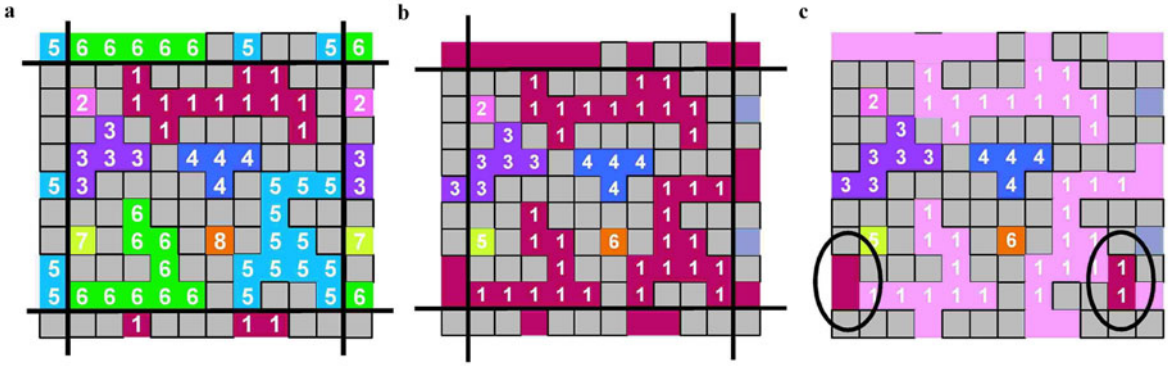


**Fig. 3** Connectivity through periodic boundary conditions. **a** Implementation of the periodic boundary conditions (PBC); **b** Connectivity through the boundaries for cluster 1; **c** Definition of percolation criterion for PBC

### 3.2 Resistance

A numerical approach similar to Argento and Bouvard [30] was choosen to calculate the one-dimensional resistance of a linear, uniform row of monosized contacting particles of the same material. The ohmic resistance between two contacting spheres can be determined in analogy to its thermal resistance, which is defined as

$$R = \frac{T_1 - T_2}{I} \tag{4}$$

with $T_1$ and $T_2$ as temperatures at the extremities of the volume and $I$ the resulting flux. The steady state calculations of the thermal resistance were performed with Ansys CFX.

Because of periodicity the FE-calculations need only to be performed for two half-spheres. Different geometries are created by increasing the particle radii while the distance $\delta$ between the two particle centers is kept constant. The contact radius can be obtained considering the respective densification approach. As the densification process in SOFC materials is geometric sintering, the contact radius $r_c^{\mathrm{SOFC}}$ is calculated geometrically from the overlapping spheres. This leads to

$$r_c^{\mathrm{SOFC}} = \sqrt{r_x^2 - \frac{\delta^2}{4}}, \tag{5}$$

where $r_x$ is the momentary particle radius (Fig. 4).

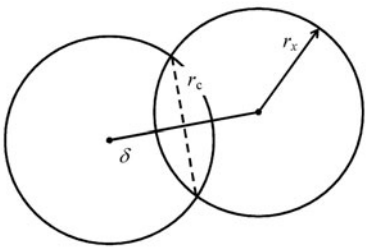


**Fig. 4** Sketch of two overlapping particles with $r_c$ as contact radius and $r_x$ as particle radius

In LIB the densification process is due to mechanical loading which is calculated in DEM assuming purely elastic behavior described by Hertz theory as described in Sect. 2. According to that, the deformation of two spheres pressed together lead to a contact radius $r_c^{\mathrm{LIB}}$ of

$$r_c^{\mathrm{LIB}} = \sqrt{r_x\left(r_x - \frac{\delta}{2}\right)}. \tag{6}$$

Calculating the flux for different particle sizes shows that the resistance $R$ normalized to the resistance of a cylinder $R_{\mathrm{cyl}}$ of radius $r_x$ and length $\delta$ increases linearly with respect to $r_x/r_c$ as shown in Fig. 5 for the geometrical contact considered in SOFC and for the Hertzian contact of LIB.

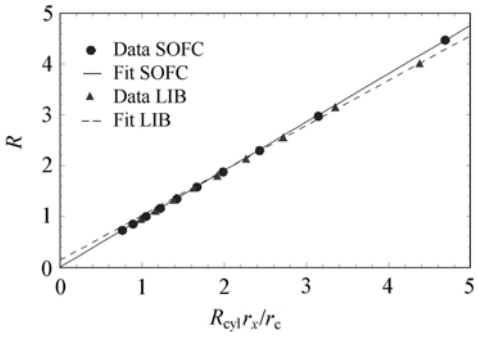


**Fig. 5** Fit function determined for different contact situations in SOFC and LIB

The following fit can be used to calculate the resistance between two particles in the SOFC microstructures

$$R = 0.952\frac{r_x}{r_c}R_{\mathrm{cyl}}. \tag{7}$$

The fit function found for Hertz contact as considered in LIB is slightly different due to the different contact situation

$$R = 0.133 + 0.887\frac{r_x}{r_c}R_{\mathrm{cyl}}. \tag{8}$$

With these equations the resistance of all contacting particles in the microstructures can be determined in dependency of particle size, contact radius and distance between particle centers. Thereby the microstructure can be transformed to an equivalent circuit.

A contact resistance either due to surface roughness or a film resistance can easily be considered by adding up an additional term in series to the resistance. However, for the methodical study performed here the contact between two particles is chosen to be ideal.

### 3.3 Network and node potential method

For this equivalent circuit a system of linear equations is set up using Kirchhoff's current law and Ohm's law considering the particles centers as nodes [31]. Thus, for node $i$ we get

$$I_i = \sum_j I_{i,j} = \sum_j \frac{V_j - V_i}{R_{ij}}, \tag{9}$$

where $I_i$ is the sum of currents between particle $i$ and it is contacting particles $j$, $V_i$ and $V_j$ are the voltages at site $i$ and $j$, respectively and $R_{ij}$ is the resistance between nodes $i$ and $j$ (Fig. 6). The sum of currents is zero for all internal nodes.

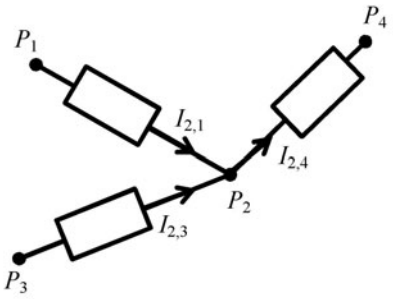


**Fig. 6** Example of equivalent circuit of a particle $P_2$ with coordination number 3

We use the node potential method to transform the linear equation system in the matrix form $\boldsymbol{KV} = \boldsymbol{I}$ where $\boldsymbol{K}$ is a symmetric matrix containing the conductivities between percolated particles in contact, vector $\boldsymbol{V}$ the unknown particle potentials and the vector $\boldsymbol{I}$ the sum of currents for each particle or respectively the source terms. The matrix $\boldsymbol{K}$ is saved in sparse form to reduce memory space.

To solve the system, potentials $\varphi_1$ and $\varphi_2$ are imposed on the opposing sides in the considered direction as boundary conditions. Thus, $\boldsymbol{K}$ and $\boldsymbol{I}$ are known, which allows $\boldsymbol{V}$ to be calculated. This is done with an iterative stabilized biconjugated gradient method (BICGSTAB) of EIGEN [32]. The potential distribution for one phase of an exemplary microstructure is shown in Fig. 7. The currents within the network can be found from back substituting particle potentials and solving Ohm's law for each contact. The total current $I$ entering or leaving the network is then calculated by adding all currents of the boundaries.

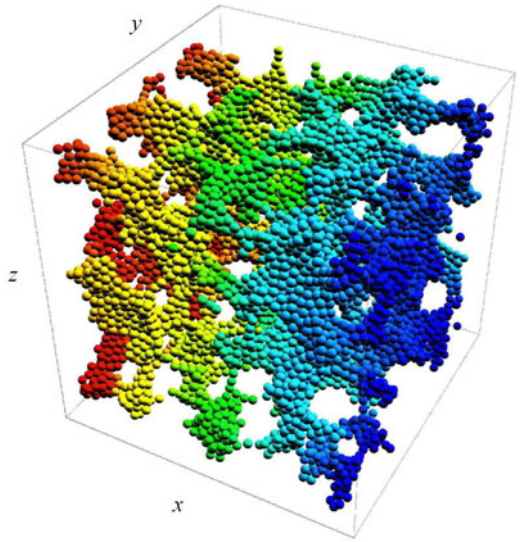


**Fig. 7** Potential distribution of one phase with an applied potential difference in $x$-direction, particles colored according to their potential

Finally, the effective conductivity $k_{\mathrm{eff},l}$ of a microstructure can be calculated normalized to its bulk conductivity $k_{\mathrm{bulk},l}$ as

$$\frac{k_{\mathrm{eff},l}}{k_{\mathrm{bulk},l}} = \frac{I}{\varphi_1 - \varphi_2} \frac{L_x}{L_y \times L_z}, \tag{10}$$

where $L_y \times L_z$ is the area of a cross-section of the box and $L_x$ the box length in the considered direction. In the following figures the conductivity is always given as the ratio of the effective conductivity $k_{\mathrm{eff},l}$ of a phase $l$ to the bulk conductivity $k_{\mathrm{bulk},l}$ of that phase $l$.

## 4 Results and discussion

As described in Ref. [30], the notion of touching particles is no longer valid at densities approaching a packing factor of 100% due to interaction of the multiple contacts. Such structure rather should be modeled as a dense matrix with distributed pores. The resistor network approach (RN) therefore overestimates the effective conductivity. It is assumed that for densities below 90% the contacts do not yet interact with each other [30]. To verify this, the effective conductivity of a monosized, single-phased cubic assembly is calculated for different packing factors. Therefore a structure of $5 \times 5 \times 5$ particles is densified by the sintering process as described in Sect. 2. The effective conductivity of the assembly normalized to the bulk conductivity is shown in Fig. 8.

Carson et al. [33] show that porous materials can be divided in granular and continuous materials by comparing their effective conductivity to the effective conductivity determined with effective media theory (EMT). EMT considers the two components to be distributed randomly in such a way that neither phase being necessarily continuous or dispersed. Therefore, the region bounded above by EMT indicates a system with continuous pore space, whereas the

region bounded below by EMT indicates a system of a continuous matrix with pore inclusions. In EMT, the calculation of the effective properties is based on the solution of the boundary value problem of a single spherical inclusion in a matrix. The surrounding matrix is of effective conductivity $k_{\text{eff}}$, which has to be determined in such a way that the perturbation of the inclusion vanishes on average for each component. For a pore space conductivity of zero the implicit relation of EMT can be simplified to

$$\frac{k_{\text{eff}}}{k_{\text{bulk}}} = 0.5(3\phi_l - 1). \tag{11}$$

It is shown in Fig. 8 that for densities of 85% the results found with RN exceed the values determined by EMT. This indicates that already for this amount of densification the notion of touching particles is no longer valid.

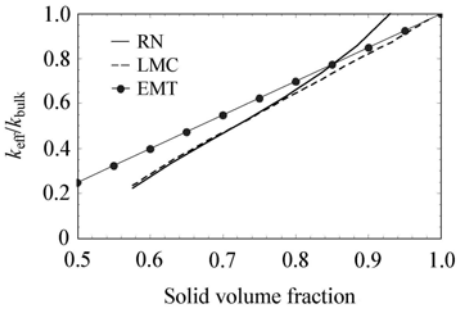


**Fig. 8** Comparison of effective conductivity from different approaches, RN: resistor network Eq. (10), LMC: lattice Monte-Carlo Eq. (13), EMT: effective medium theory Eq. (11)

For validation of the approach, the results are compared to values determined with a LMC approach. LMC is a well established approach for the determination of heat transport problems on a discretizised structure of a random assembly [12]. Due to the discretization of the structure the approach is valid for all states of densification. With the help of random walk simulations the effective diffusivity of a porous medium can be determined: for a large number of tracer particles performing random walk movements in the relevant phase $l$, the mean square displacement is monitored over time. The Einstein equation describes the self-diffusivity D of randomly walking particles in relation to the mean square displacement $\langle u^2 \rangle$ of the particles by

$$D_{\text{eff},l} = \frac{\langle u^2 \rangle}{6t}, \tag{12}$$

where $t$ is the average travel time. Based on the effective diffusivity, the effective conductivity can be determined according to Tobochnik et al. [34] for a phase $l$ as

$$k_{\text{eff},l} = \frac{D_{\text{eff},l}}{D_{\text{bulk},l}}[\phi_l(1-\epsilon)P_l], \tag{13}$$

where $\epsilon$ is the porosity of the assembly and $P_l$ the percolation probability.

The comparison of the results (Fig. 8) lead to the same conclusion: below densities of 85% the difference of the results between LMC and RN is marginal, rendering the RN approach suitable. For densities exceeding 85%, RN overestimates conductivity with respect to LMC. This leads to the assumption that RN is a feasible approach for relative densities below 85%. As both LIB and SOFC require connected pore space to sustain electrolyte or gas transport, it is justified to investigate their structures by RN as they will have relative densities below 85%.

### 4.1 Applications in SOFC

As described in Sect. 2, SOFC electrodes are considered in this work as a mixture of ionic (YSZ) and electronic (Ni) conducting phases. In the results shown here, Ni is always assumed to be the small particle, even though this could be reversed.

The average percolation probability obtained with the Hoshen–Kopelman algorithm is shown in Fig. 9a for several volume fractions and size ratios from 1 to 10. Exchanging YSZ and Ni in the results would lead to a size ratio from 1 to 0.1. Depending on average particle size, either the first or the second range is more relevant to improve cell performance [3]. However, for a methodological comparison, as done in this work, it is sufficient to focus on one range.

For comparison the percolation probability calculated with percolation theory in accordance to Ref. [6] is shown in Fig. 9b. Our method described in Sect. 3.1 leads to a larger range in which both Ni and YSZ phase are percolated than the percolation theory. Especially for large size ratios the deviation is significant. There are three possible reasons for this:

(1) The correlation between percolation probability and coordination number $Z_{l,l}$ was derived by investigating microstructures which were numerically generated in a way that ensures the average coordination number $Z_0$ to be 6 [6]. Therein $Z_0$ is the average overall number of contacts of a particle. In Fig. 10 the coordination numbers of all densified microstructures considered in this work are shown. The average coordination number is equal to 6 only for a small range of compositions, for most structures it is found to exceed 7. A variation in average coordination number for different volume fractions in binary mixtures was already reported by Bertei and Nicolella [35]. In contrast to our results the coordination numbers found in their work are below 6 as they consider undensified structures.

(2) The percolation threshold is assumed to correlate to a certain coordination number $Z_{l,l}$, which was first estimated to be 2 [6] for size ratios below 3. Kuo and Gupta [36] found a coordination number of 1.764 to be in better agreement with numerical simulations for a range of size ratios from 0.154 to 6.464. To examine this, the percolation probabilities found with the Hoshen–Kopelman algorithm are plotted versus the coordination number $Z_{\text{Ni,Ni}}$ and $Z_{\text{YSZ,YSZ}}$ in Fig. 11 for several size ratios. The percolation threshold takes place for coordina-

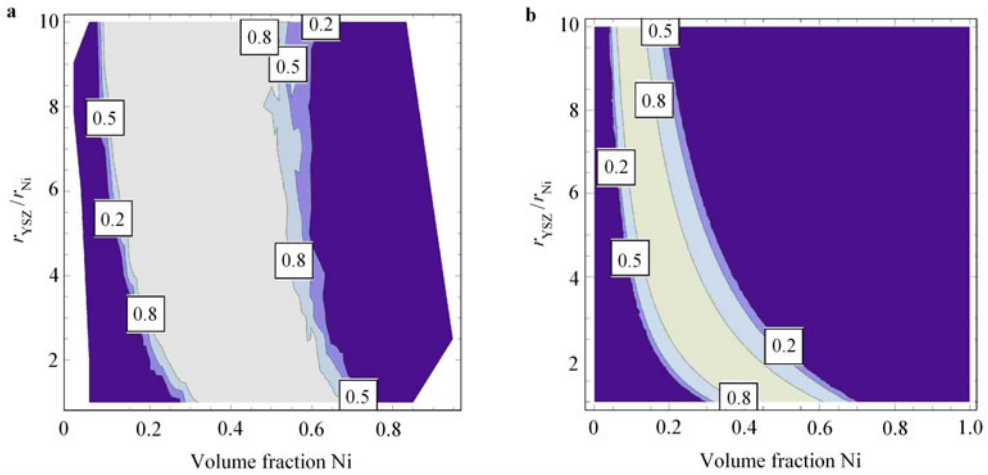


**Fig. 9** Percolation probability [36] calculated with **a** Hoshen–Kopelman algorithm as described in Sect. 3.1 and **b** percolation theory for size ratios from 1 to 10 and solid volume fractions of Ni from 0 to 1 in accordance to Bouvard [6]

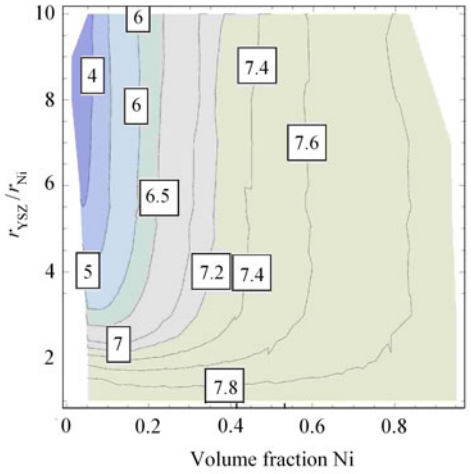


**Fig. 10** Average coordination numbers of the densified assemblies. The packing algorithm used in this work does not guarantee that all particles are in contact with other particles. Those without contact are not considered in the calculation of coordination numbers

tion numbers $Z_{Ni,Ni}$ between 2 and 3 for the small Ni particles, whereby the critical coordination number clearly increases with increasing particle size ratio. The critical coordination number $Z_{YSZ,YSZ}$ scatters diffusely around 2 for the large YSZ particles. The scattering for the large particles might be due to the fact, that the assemblies contain too little large particles for high size ratios. The clear distribution of percolation threshold for small particles indicates that it is not feasible to correlate the percolation threshold to a single value of coordination number $Z_{l,l}$ as it is done so far. Rather it might depend on further parameters such as size ratio, method for generation of the microstructure or densification. As the number of small particles within the investigated representative volume increases with increasing size ratio, there might be a dependence on the number of particles in the investigated representative volume size.

(3) The generated assemblies contain 10 000 particles, which leads to a rather low amount of large particles for high size ratios, especially for high volume fractions of Ni. For example at a radius ratio of 8 the assemblies with the critical solid volume fraction 0.1 for percolation of Ni contain 156 large particles, whereas at the critical volume fraction 0.55 for percolation of YSZ they contain only 16 particles. In Fig. 12 the standard deviation in percolation probability for all 10 assemblies of the same composition is shown for all volume fractions for radius ratio 1 (R1) and radius ratio 8 (R8). The percolation threshold takes place at a critical volume fraction below which no connectivity is found (percolation probability = 0) and above which the percolation probability quickly approaches 1. At the critical volume fraction itself it is very likely to find a large deviation within the percolation probability. A single peak in the standard deviation of percolation probability, as found for the small particles in R8 (Fig. 12a) indicates a high accuracy of the determined percolation threshold. For the other cases in the example the values scatter about a median, especially for the large particles in R8 (Fig. 12b) the dispersion with respect to the volume fraction is wide. Although this dispersion could be reduced with either more or larger assemblies, 10 assemblies off 10 000 particles were considered to be sufficient as a trade of between accuracy and computational costs.

Based on the information on connectivity within the clusters, the effective conductivity is calculated for all assemblies by our RN method. As an example, the conductivities of the two phases for structures with particle size ratio YSZ to Ni of 5 are shown in Fig. 13. Here again ten assemblies of each composition are analyzed for statistical purpose and the mean values of the conductivity of the large and small particles (YSZ and Ni, respectively) are calculated. Let us first compare in Fig. 13 the mean conductivities found with RN and LMC to estimate the systematic deviation due to methodical differences. The predicted tendency

of increasing conductivity with increasing volume fraction is similar. The absolute error $|k_{\mathrm{eff,RN}} - k_{\mathrm{eff,LMC}}|$ is less than 0.02 for the YSZ particles corresponding to a relative deviation $|k_{\mathrm{eff,RN}} - k_{\mathrm{eff,LMC}}|/k_{\mathrm{eff,LMC}}$ of 5% to 9% and it is less than 0.014 for the Ni particles equaling a relative error of 5% to 7%. The small deviation between the mean values of the two approaches confirms that the results found with the faster RN approach are in reasonable agreement with the values from LMC. Thus, RN is suitable for the determination of the effective conductivities of separate phases in densified structures. Next, these results are compared to values obtained with EMT (Eq. (11)) and the adjusted Bruggeman equation [6] (Eq. (1)). The effective conductivities of all volume fractions are bound above by EMT, indicating the loose granularity of this phase. For the large YSZ particles the difference between RN and the percolation approach is quite large. As mentioned before there is a deviation between the percolation probabilities found with percolation theory and with the Hoshen–Kopelman algorithm. As percolation probability is considered in the adjusted Bruggeman equation, this can explain the deviation partly. The overall coordination number found in the generated microstructures is unequal to the assumed value in percolation theory; the percolation threshold found with HK varies in contrast to the constant value in percolation theory for larger size ratios and the small amount of large particles combined with the periodicity of the assembly reduces the randomness of the considered structures. This leads to a large deviation in the onset of conductivity as the percolation threshold found with percolation theory according to [6] is 0.3 volume fraction and around 0.6 with HK. Additionally to percolation probability, in solutions found with the adjusted Bruggeman equation a constant porosity of 0.4 is assumed whereas in the generated microstructures porosity varies between 0.15 and 0.25. For the small Ni particles percolation theory predicts only slightly larger values for the effective conductivity, whereby the deviation is larger for smaller volume fractions of Ni. EMT estimates a rather different behavior for the effective

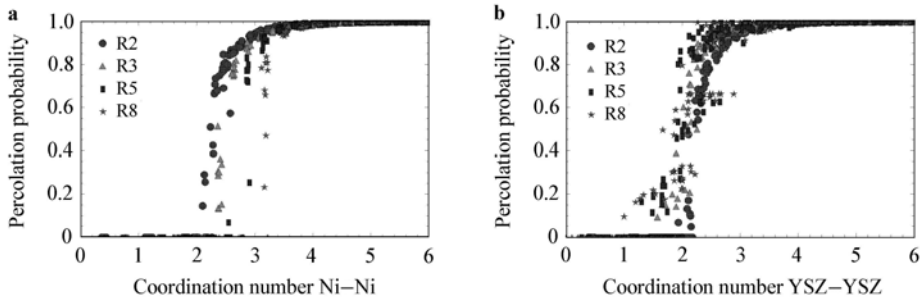


**Fig. 11** Percolation probability versus coordination number **a** $Z_{\mathrm{Ni,Ni}}$ and **b** $Z_{\mathrm{YSZ,YSZ}}$ for several size ratios from R1: $r_{\mathrm{YSZ}}/r_{\mathrm{Ni}} = 1$ to R8: $r_{\mathrm{YSZ}}/r_{\mathrm{Ni}} = 8$

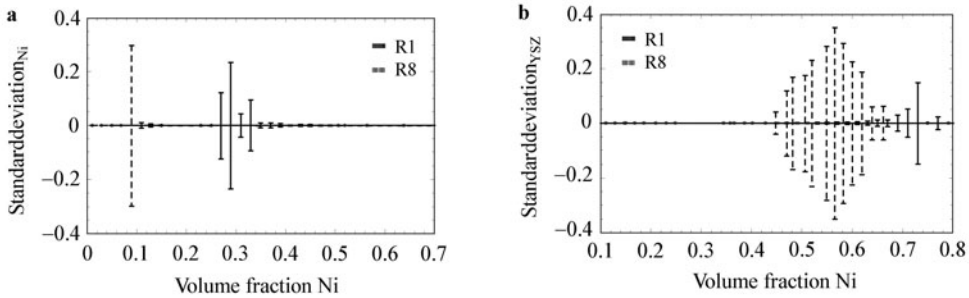


**Fig. 12** Standard deviation in percolation probability versus volume fraction for **a** Ni and **b** YSZ for two size ratios R1: $r_{\mathrm{YSZ}}/r_{\mathrm{Ni}} = 1$ and R8: $r_{\mathrm{YSZ}}/r_{\mathrm{Ni}} = 8$

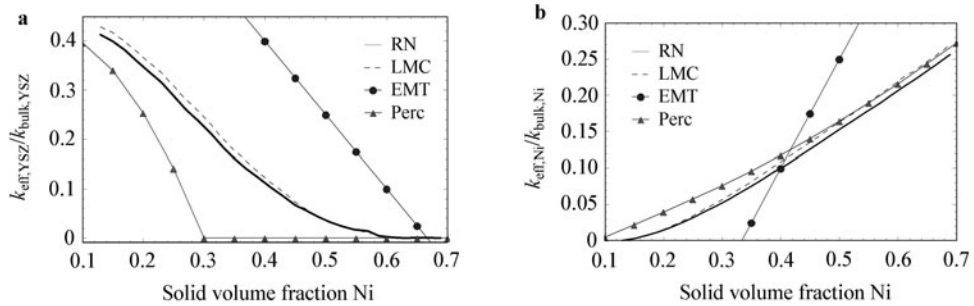


**Fig. 13** Effective conductivity calculated with resistor network approach (RN) compared to results from a LMC approach for **a** YSZ and **b** Ni

conductivity compared to RN and LMC. As the percolation threshold differs for the two phases of the system, the structures can not be considered as symmetric and therefore EMT is not applicable to predict the percolation threshold correctly for both phases [4]. The large deviation between the results of averaging approaches (EMT and Bruggeman) and found based on existing structures (RN and LMC) shows the importance of the later methods for the understanding of the influence of microstructure on effective transport properties.

In Fig. 14 the standard deviations of the results are given for the 10 assemblies of each composition. The deviation within the LMC method is slightly shifted to the left for better visibility. The deviation in the conductivities of the same composition is due to the variation in microstructure of the randomly generated distributions. The standard deviation for LMC is in most cases insignificantly larger than the values of the RN approach. This difference might be caused by the averaging over a certain number of time steps in LMC and is assumed to vanish with increasing time. For the large YSZ particles the standard deviation is below 2% for all compositions and for the small Ni particles it is an order of magnitude smaller. The difference between the standard deviations of YSZ and Ni is due to the fact the amount of small particles is larger than the number of large particles within the structure. As the standard deviation is reasonable small for both species, the assembly size can be considered to be sufficient.

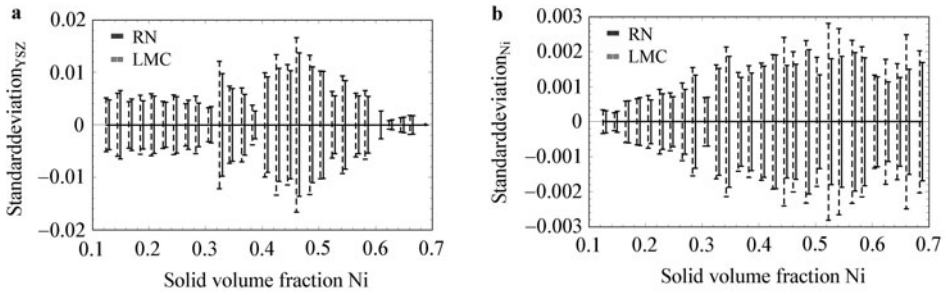


**Fig. 14** Standard deviation within the effective conductivities calculated with resistor network approach (RN) and LMC approach for the 10 microstructures of each composition for **a** YSZ and **b** Ni

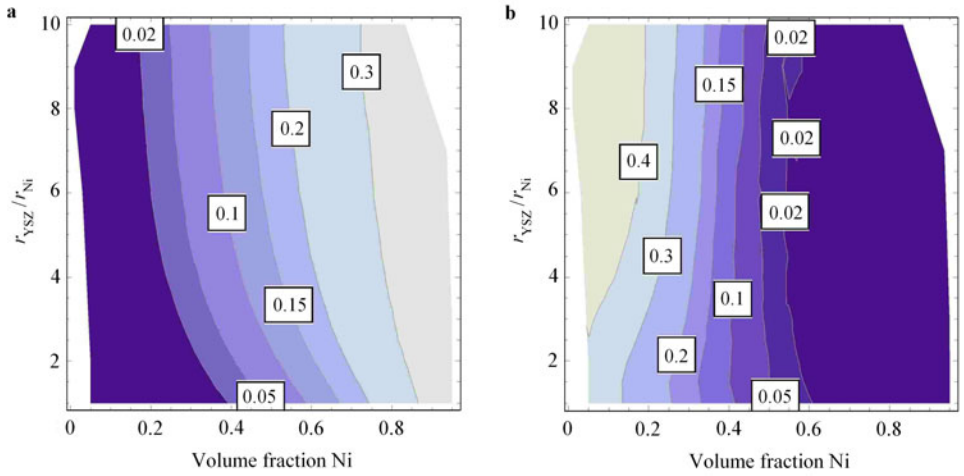


**Fig. 15** Effective conductivity of **a** Ni and **b** YSZ

Finally, the effective conductivities of the various assemblies for size ratios from 1 to 10 are shown in Fig. 15a for the Ni phase (small particles) and in Fig. 15b for the YSZ phase (large particles). In accordance with averaging methods, effective conductivity increases with the volume fraction for both species. Furthermore, there is also a slight increase with size ratio, which is not considered in averaging methods in general.

The results shown here can be used to increase the accuracy of studies on the optimization of microstructure with regards to cell power density such as Refs. [2, 3].

### 4.2 Applications in lithium ion batteries

As shown previously, the proposed method is suitable for the determination of effective conductivity in densified, granular materials. Therefore, it was also applied for the investigation of the impact of microstructural changes on effective conductivity in LIB.

As mentioned before, carbon black (CB) is added to enhance electronic conductivity of the electrode structure. Therefore it is important to understand how and in

which amount it contributes to this, especially when the active material (AM) under consideration is a bad electron conductor such as $Li_xMn_2O_4$ or $Li_xFePO_4$ [1]. It was shown by Dominko et al. [36] that with a decreasing amount of CB there is an abrupt decrease in the electronic conductivity directly correlated to cell capacity: without percolation less and less active particles are supplied with electrons and therefore cannot participate in the intercalation/deintercalation process. On the other hand it is desirable to minimize the content of CB as much as possible with regard to energy density [38]. In different studies the content of added CB, $\omega$(CB), varies from 5% to 30%. Tarascon and Guyomard [39] found that the optimized amount of CB, $\omega$(CB), should between 5% and 10%, corresponding to solid volume fractions between 3.15% and 6.3% for an active particle size around 2 µm and a corresponding size ratio of 50. Hellweg [40] on the other hand found that the percolation threshold for CB in Lithium Ion Batteries is between 10% and 13% solid volume fraction for electrodes with a particle size ratio of 2. Due to the lack of further data, we assume that the percolation threshold for electrode structures with a size ratio of 10 is between those values.

As described in Sect. 2 different configurations have been generated (Table 1) and further densified by DEM modeling. The used material parameters for the DEM simulations are given in Table 2. The average stress $\sigma_{ij}$ developed in the microstructure can be calculated by summing up all existing contact pairs

$$\sigma_{ij} = \frac{1}{L_x \times L_y \times L_z}\left( \sum_{I<J} \delta^{I,J} f_n^{I,J} n_i n_j + \sum_{I<J} \delta^{I,J} f_t^{I,J} n_i t_j \right). \quad (14)$$

Here, $f_n^{I,J}$ and $f_t^{I,J}$ are the normal and tangential forces applied from particle $J$ on particle $I$, $\delta^{I,J}$ denotes the distance between the centers of the particles and the unit vectors $n_i$ and $t_j$ are the normal and tangential unit vectors of the contact, respectively [24].

First, the influence of initial $PF$ and composition is investigated for the intercalation process. As the system is quasi-isotropic, only mean values are compared for the different microstructures. The mean hydrostatic stress developing as a consequence of the volume increase is shown in Fig. 16 for the different compositions. As can be expected, higher volume fractions of AM lead to higher stresses within the samples both for low (Fig. 16a) and high (Fig. 16b) packing factors. The influence of the initial $PF$ on the hydrostatic stress developed during intercalation is quite low: for the high $PF$ the maximal stress is between 2.5 and 3 MPa higher than the stress for the equivalent composition with low value of $PF$.

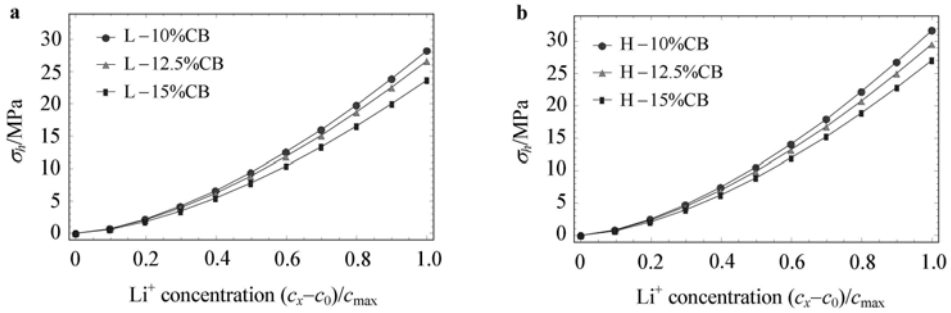


**Fig. 16** Development of hydrostatic stress during intercalation process for **a** low initial packing factor 67.3% (L) and **b** high initial packing factor 69.4 (H) for compositions with solid volume fractions of carbon black (CB) between 10% and 15%

The change in conductivities normalized by its bulk conductivities during intercalation process is calculated for the changing microstructures as shown for AM in Fig. 17 and CB in Fig. 18 separately. Obviously, the ion transport mainly takes place in the electrolyte. AM is always percolated as the considered volume fractions are above the expected percolation threshold. The increase in effective conductivity during the intercalation process is due to the increasing contact forces between the particles. The contact area increases with the normal force $f_n$ in accordance to Hertz' law with $r_c \propto f_n^{1/3}$. As expected, a higher volume fraction of AM leads in general to a higher effective conductivity in that phase. The absolute deviation in the maximal values for low and high $PF$ is around 0.02 correlating to a relative deviation of 12%.

CB only percolates for volume fractions of 15% for the densification process considered here. The $PF$ influences the concentration level for which percolating clusters are found only rarely: for a low initial $PF$ the onset of conductivity in the CB phase is around 60% of the maximal possible $Li^+$ concentration $c_{max}$ (Fig. 18a) and for high $PF$s it is around 50% $c_{max}$ (Fig. 18b). The maximal normalized effective conductivity in CB is 0.007 for the high value of $PF$ and 0.006 for a low PF, this corresponds to a relative deviation of 14%.

As mentioned in Sect. 1 the effective conductivity used in the Dual–Foil model is usually determined by a Bruggeman approach. As this approach does not consider percolation behavior, we use the Bruggemann approach weighted with percolation probability (Eq. (1)) for comparison. In Fig. 19 the values obtained for the maximal $Li^+$ concentration $c_{max}$ for the compositions with high initial packing factor (LIB) are compared to the weighted Bruggeman approach

(Perc) and additionally to results gained for sintered structures with size ratio 10 in Sect. 4.1 (SOFC). The percolation threshold determined with percolation theory [6] is predicted to be less than 5% for a radius ratio of 10, while with our method described in Sect. 4.1 we obtain a percolation threshold around 10% volume fraction of small particles for sintered structures with size ratio 10. Not only the percolation threshold differs substantially for the different methods, but also the conductivities obtained for the structures densified with DEM are significantly lower than the values obtained with other approaches. This is due to the fact that the contact area described with Hertz' law is in general smaller than the contact area in sintered structures. The large difference between the results for LIB and SOFC shows the importance of considering the densification process.

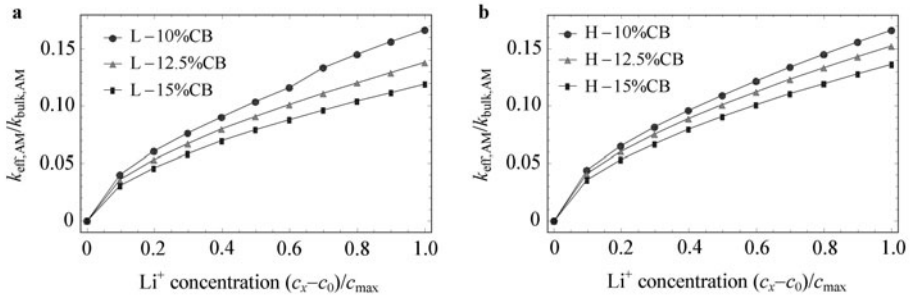


**Fig. 17** Development of effective conductivity of the active material AM normalized by its bulk conductivity during intercalation for **a** low initial packing factor (67.3%) and **b** high initial packing factor (69.4%)

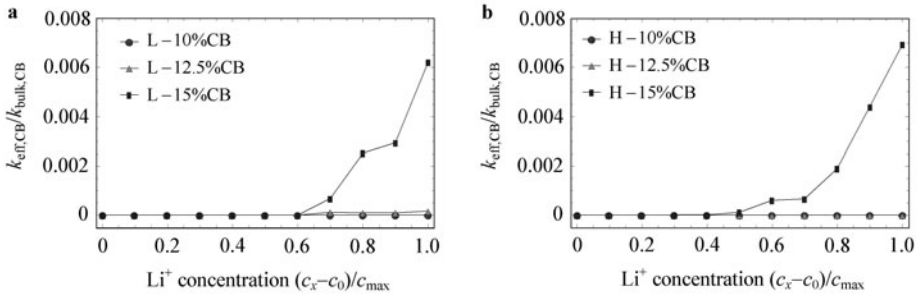


**Fig. 18** Development of effective conductivity of carbon black normalized by its bulk conductivity during intercalation for **a** low initial packing factor (67.3%) and **b** high initial packing factor (69.4%)

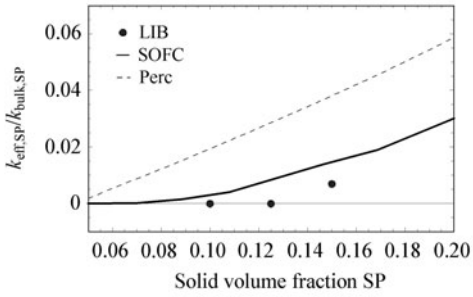


**Fig. 19** Effective conductivity for microstructures densified with DEM (LIB), numerical sintering (SOFC) and from percolation theory (Perc) for a size ratio of 10

Furthermore, the percolation threshold for CB found numerically is above the experimentally determined values [41] even though we expected it to be lower as the size ratio in the numerical structures is higher. One possible reason for the deviation could be that we have not considered until now that the manufactured electrode structures in Ref. [41] have been compressed prior to measuring the conductivity. Since in general the electrode structures are calendered during manufacturing, this pre-loading will be considered in the following analysis. To investigate the impact of the calendering step, we load the microstructures with a combined process of compression and intercalation. As an example the development of stresses in *x*-, *y*- and *z*-direction of the microstructures with 10% solid volume fraction CB and a high initial *PF* of 69.4% is shown in Fig. 20 for the combined cal-

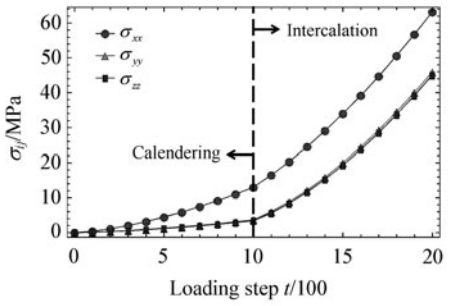


**Fig. 20** Stress developing with incremental time step for the combined calendering and intercalation process in microstructures with 10% volume fraction carbon black and high initial packing factor 69.4%

endering and intercalation process. Uni-axial load is applied during the first 10 loading steps in $x$-direction and intercalation induced volume increase for the last 10 loading steps, as indicated in the picture. The uni-axial compression leads to a strongly anisotropic behavior with higher stress $\sigma_{xx}$ in loading direction, whereas in perpendicular directions the stresses $\sigma_{yy}$ and $\sigma_{zz}$ are similar. The anisotropy induced during calendering is not reduced during the intercalation process. Due to the non-linear mechanical behavior of the system, the stress increases more in the pre-calendered case during the intercalation process with $\Delta\sigma_{xx} = 45.8$ MPa and $0.5(\Delta\sigma_{yy}+\Delta\sigma_{zz}) = 35.5$ MPa than in the non-calendered case with $\sigma_h = 31.7$ MPa in all directions.

As the same trends in the development of stress and connectivity are found for the here considered structures both with low and high *PF*s and the deviation resulting from the different *PF*s is insignificant, we only consider the compositions with high initial packing factor (H) in the following simulations. Again the results are average values of three microstructures for each composition. In Fig. 21 the increase of stress during the intercalation process in $x$-, $y$- and $z$-direction is shown separately for each composition. The initial stress due to calendering is between 11 MPa and 13 MPa for all assemblies in $x$- direction and around between 3 MPa and 4 MPa in the perpendicular directions. The anisotropy due to calendering is not reduced for any of the microstructures during the intercalation process. Even though the tendency of increasing stress with increasing volume fractions of active material is the same for calendered and non-calendered assemblies during intercalation, the increase in stress is higher for all pre-calendered assemblies in comparison with the non-calendered counterparts, in load direction up to 20 MPa, in perpendicular directions around 10 MPa.

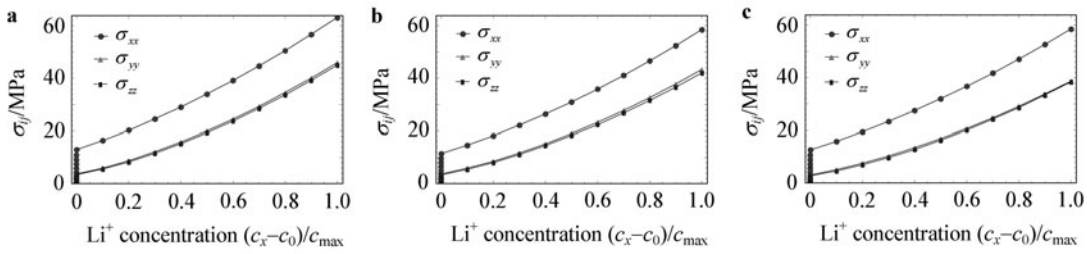


**Fig. 21** Stress developing with normalized concentration for microstructures with high packing factor (69.4%) and **a** 10% volume fraction carbon black (CB); **b** 12.5% volume fraction CB and **c** 15% volume fraction CB

Since the RN method we use already obtains information on the directional dependency of the conductivity, the method is applicable for anisotropic microstructures without any further adaptation. The impact of calendering on the effective conductivity can be estimated by comparing the results for the intercalation process for the calendered and non-calendered structures. For the AM phase, the anisotropic stress leads to anisotropic conductivity in all cases (Figs. 22a–22c). The retaining of anisotropy during the intercalation process indicates that little rearrangement within this phase takes place. Compared to the non-calendered cases, which are shown in Figs. 22d to 22f, two positive effects induced by the calendering can be seen. First, the initial conductivity is greater than zero due to the pre-loading. Second, the conductivity in general reaches higher values for the calendered cases. The amount of increase in conductivity during the intercalation process is with 10% of the bulk conductivity lower compared to the non-compressed cases with a maximal effective conductivity between 14% and 17% of the bulk conductivity. Conversely the increase in stress during intercalation is higher for the calendered cases.

Further, the conductivities of the CB phase are given for the calendered configurations in Figs. 23a–23c and for the non-calendered structures in Figs. 23d–23f. Comparing the calendered compositions to the non-calendered, there are 2 advantages. First, percolation paths are already formed before the intercalation process starts due to the pre-load. This shows the importance of the calendering process for proper cell performance. Furthermore, percolation is already found for 12.5% volume fraction CB (Fig. 23b), which is closer to the expected values. Remaining deviations of the numerical results from the experiments might be caused by the approximations made in the mechanical modeling: to reduce computational costs the particle shape is idealized to be spherical and additionally the influence of binder on the homogeneous particle distribution is not considered. In future work the influence of this aspects can be considered to obtain a more accurate mechanical behavior.

In contrast to the AM, no clear preferential direction is found for the calendered CB phase. For 15% solid volume fraction CB the effective conductivities in $y$-direction are similar and even higher than the conductivities found in $x$-direction. For 12.5% solid volume fraction CB the averaged conductivities are largest in loading direction in loading direction (Fig. 23b). However, among the the three different microstructures of that composition the preferential directions of conductivity vary substantially as shown in Table 3 exemplary for the maximal Li$^+$ concentration $c_{max}$ at the end intercalation.

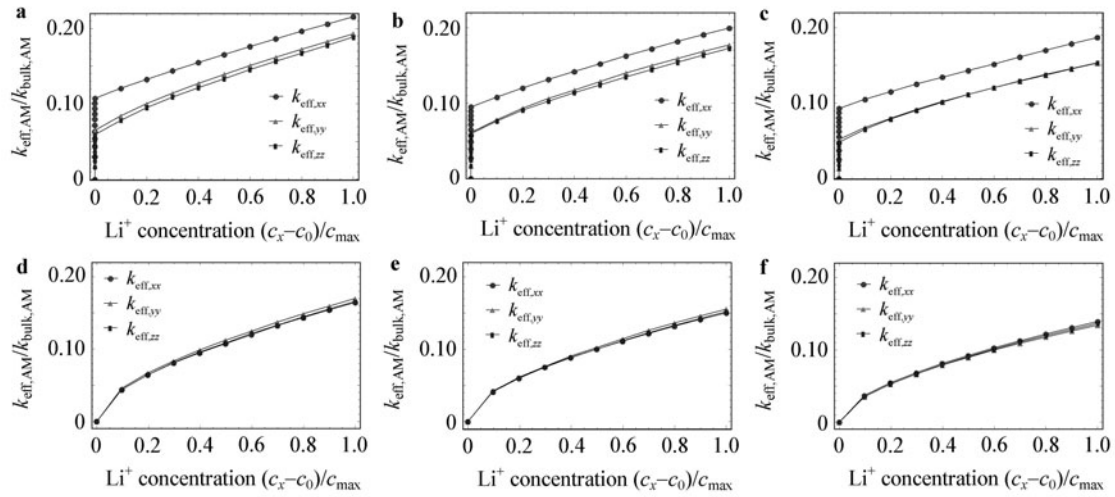


**Fig. 22** Change in conductivity for active material (AM) during intercalation process for the pre-calendered cases in **a** to **c** and the non-calendered cases in **d** to **f** for different volume fractions carbon black (CB). **a** 10% volume fraction (CB); **b** 12.5% volume fraction CB; **c** 15% volume fraction CB; **d** 10% volume fraction (CB); **e** 12.5% volume fraction CB; **f** 15% volume fraction CB

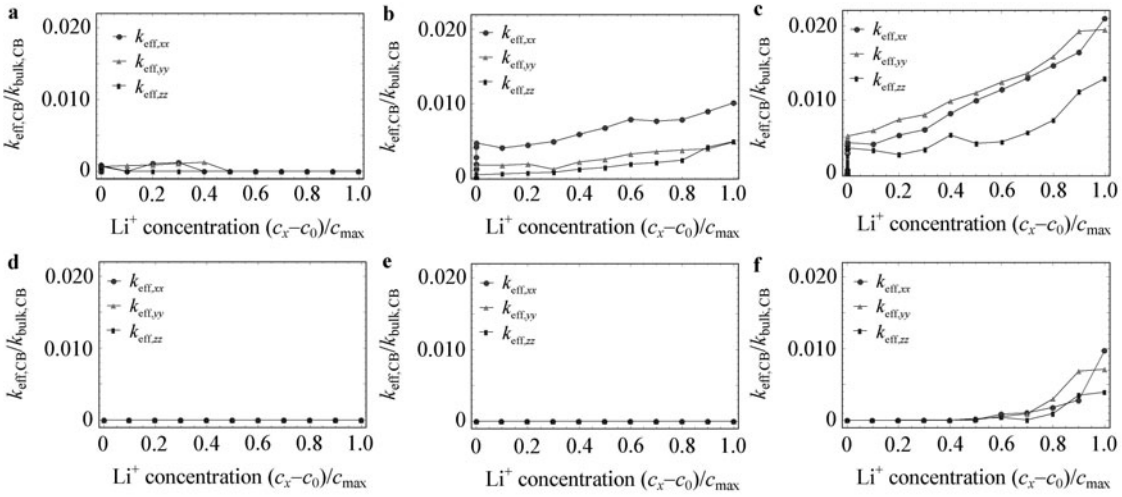


**Fig. 23** Change in conductivity for carbon black (CB) during intercalation process for the pre-calendered cases in **a** to **c** and the non-calendered cases in **d** to **f** for different volume fractions of CB. **a** 10% volume fraction (CB); **b** 12.5% volume fraction CB; **c** 15% volume fraction CB; **d** 10% volume fraction (CB); **e** 12.5% volume fraction CB; **f** 15% volume fraction CB

**Table 3** Relative effective conductivity of carbon black for the 3 different assemblies (1, 2, 3) with 12.5% volume fraction of carbon black at the end of the intercalation process

| | 1 | 2 | 3 |
|---|---|---|---|
| $\frac{3k_{eff,xx}}{k_{eff,xx}+k_{eff,yy}+k_{eff,zz}}$ | 0.594 | 1.421 | 0.985 |
| $\frac{3k_{eff,yy}}{k_{eff,xx}+k_{eff,yy}+k_{eff,zz}}$ | 2.644 | 0.100 | 0.256 |
| $\frac{3k_{eff,zz}}{k_{eff,xx}+k_{eff,yy}+k_{eff,zz}}$ | 1.099 | 0.614 | 1.287 |

This observation can be explained as follows: as described in Ref. [41] the large particles (AM) form a force carrying backbone within the assembly, whereas the small particles (CB) fill the interstitial space between the larger particles. The formation of a force carrying structure is favored as AM is rigid compared to CB. Therefore, the CB particles are more likely to rearrange and reduce the anisotropy during the intercalation process. To investigate that, we calculated the stress and movement for large and small particles separately for one exemplary structure. The average movement of large and small particles is quasi-isotropic during the intercalation process. Small particles have an average movement of 0.01% of the box length, which is twice as much as

large particles have. The stresses for AM and CB shown separately in Fig. 24a and Fig. 24b confirm the assumption that the large particle are force carrying: the stress in the AM cluster is in the same order of magnitude as the overall stress with a maximal stress in loading direction of the compression. In contrast, the stress in the CB cluster is several orders of magnitude lower and does not develop a maximum stress in the loading direction.

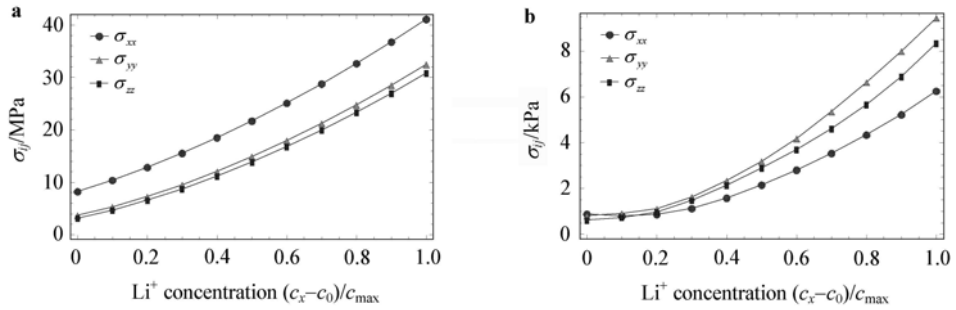


**Fig. 24** Development of stress during intercalation process for **a** large active material particles and **b** small Carbon Black particles separately

## 5 Conclusion

In this work, a fast and flexible resistor-network method (RN) for the calculation of effective conductivities in granular electrode structures has been introduced. As the conductivity can be calculated for different directions, the method is applicable for densified structures with and without preferential direction. The method was validated by comparison to results obtained by the established lattice Monte Carlo approach. The findings for both methods are in good agreement for isotropic assemblies and the RN approach is less time consuming. Contrary to the RN method, the lattice Monte Carlo approach is not applicable for assemblies with a preferential direction without further adaption.

We have studied systematically the influence of morphology on connectivity and conductivity with regard to SOFC. An enlarged percolation area was found, especially for large size ratios. In contrast to former findings the percolation threshold does not correlate independently of particle size ratio to a fixed value of the coordination number, but rather varies with size ratio. The effective conductivity shows an increase with volume fraction as expected and additionally, an increase with size ratio. As the consideration of more realistic microstructures in our study lead to different results compared to those with percolation theory, they can be used as to increase the accuracy in studies with porous electrode theory.

Furthermore, we investigated the influence of intercalation induced stress and calendering on the effective conductivity in LIB electrodes, in particular with regard to the electron conducting CB phase. In general, an increase of conductivity during the intercalation process was observed in analogy to increasing contact forces. The positive influence of calendering on the percolation threshold and the effective conductivity was shown. The calculated properties can be used to improve cell level modeling.

**Acknowledgement** The project is supported by the Helmholtz Portfolio "elektrochemische Speicher", particularly the work related to lithium-ion batteries. The work related to SOFC was partially supported as part of the HeteroFoam Center, an Energy Frontier Research Center funded by the U.S. Department of Energy, Office of Science, Basic Energy Sciences (DE-SC0001061). Banjamin Völker and Robert M. McMeeking acknowledge support from the Center for Scientific Computing at the CNSI and MRL: an NSF MRSEC (DMR-1121053) and NSF (CNS-0960316). Yixiang Gan acknowledges Australian Research Council Grant DE130101639.

## References

1 Awarke, A., Lauer, S., Pischinger, S., et al.: Percolation-tunneling modeling for the study of electric conductivity in $LiFePO_4$ based Li-ion battery cathodes. Journal of Power Sources **196**, 405–411 (2011)
2 Chen, D., Lin, Z., Zhu, H., et al.: Percolation theory to predict effective properties of solid oxide fuel-cell composite electrodes. Journal of Power Sources **191**, 240–252 (2009)
3 Völker, B., McMeeking, R.M.: Impact of particle size ratio and volume fraction on effective material parameters and performance in solid oxide fuel cell electrodes. Journal of Power Sources **215**, 199–215 (2012)
4 Torquato, S.: Random heterogeneous materials: Microstructure and macroscopic properties. In: Interdisciplinary Applied Mathematics. Springer, New York (2002)
5 Ferguson, T.R., Bazant, M.Z.: Nonequilibrium thermodynamics of porous electrodes. Journal of Electrochemical Society **159**, A1967–A1985 (2012)
6 Bouvard, D., Lange, F.: Relation between percolation and particle coordination in binary powder mixtures. Acta Metall. Mater. **39**, 3083–3090 (1991)
7 Costamagna, P., Costa, P., Antonucci, V.: Micro-modelling of solid oxide fuel cell electrodes. Electrochimica Acta **43**, 375–394 (1998)
8 Choi, H.W., Gawel, D., Berson, A., et al.: Comparison between FIB-SEM experimental 3-d reconstructions of SOFC

electrodes and random particle-based numerical models. ECS Transactions **35**, 997–1005 (2011)
9 Schneider, L., Martin, C., Bultel, Y., et al.: Discrete modelling of the electrochemical performance of SOFC electrodes. Electrochimica Acta **52**, 314–324 (2006)
10 Abel, J., Kornyshev, A., Lehnert, W.: Correlated resistor network study of porous solid oxide fuel cell anodes. Journal of Electrochemical Eociety **144**, 4253–4259 (1997)
11 Chen, Y.H., Wang, C.W., Liu, G., et al.: Selection of conductive additives in liion battery cathodes. Journal of the Electrochemical Society **154**, A978–A986 (2007)
12 Völker, B., McMeeking, R.M.: The effect of pore-former particles on microstructural features and electrochemical performance in solid oxide fuel cell electrodes. Journal of Power Sources **4**, 15.1–15.23 (2013)
13 Sunde, S.: Simulations of composite electrodes in fuel cells. Journal of Electoceramics **5**, 153–182 (2000)
14 Doyle, C.M.: Design and simulation of lithium rechargeable batteries. [Ph.D. Thesis], University of California, Berkeley (1995)
15 Zinchenko, A.Z.: Algorithm for random close packing of spheres with periodic boundary conditions. Journal of Computational Physics **114**, 298–307 (1994)
16 Jodrey, W., Tory, E.: Computer simulation of close random packing of equal spheres. Pysical Review A **32**, 2347–2351 (1985)
17 Torquato,S., Truskett, T.M., Debenedetti, P.: Is random close packing of spheres well defined? Physical Review Letters **84**, 2064–2067 (2000)
18 Xu, N., Blawzdziewicz, J., O'Hern, C.S.: Random close packing revisited: Ways to pack frictionless disks. Physical Review E **71**, 061, 306–1–061, 306–9 (2005)
19 Gan, Y., Kamlah, M., Reimann, J.: Computer simulation of packing structure in pebble beds. Fusion Engineering and Design **85**, 1782–1787 (2010)
20 Lanzini, A., Leone, P., Asinari, P.: Microstructural characterization of solid oxide fuel cell electrodes by image analysis technique. Journal of Power Sources (2009)
21 David, W., Thackery, M., Picciotto, L.D., et al.: Structure refinement of the spinel-related phases $Li_2Mn_2O_4$ and $Li_{0.2}Mn_2O_4$. Journal of Solid State Chemistry **67**, 316–323 (1987)
22 Beattie, S., Larcher, D., Morcrette, M., et al.: Si electrodes for Li-ion batteries—a new way to look at an old problem. Journal of Electrochemical Society **155**, A158–A163 (2008)
23 Zheng, H., Tan, L., Liu, G., et al.: Calendering effects on the physical and electrochemical properties of $Li[Ni_{1=3}Mn_{1=3}Co_{1=3}]O_2$ cathode. Journal of Power Sources **208**, 52–57 (2012)
24 Gan, Y., Kamlah, M.: Discrete element modelling of pebble beds: With application to uniaxial compression tests of ceramic breeder pebble beds. Journal of Mechanics and Physics of Solids **58**, 129–144 (2010)
25 Zhang, X., Shyy, W., Sastry, A.: Numerical simulation of intercalation-induced stress in Li-ion battery electrode particles. Journal of the Electrochemical Society **154**, A910–A916 (2007)
26 Leisen, D.: Nanoindentierung als Methode zur mikromechanischen Charakterisierung von Li-Batteriewerkstoffen. [Master Thesis], Karlsruhe Institute of Technology (KIT), German (2010)
27 Al-Futaisi, A., Patzek, T.: Extension of Hoshen–Kopelman algorithm to non-lattice environments. Physica A **231**, 665–678 (2003)
28 Metzger, T., Irawan, A., Tsotsas, E.: Remarks on the paper "Extension of Hoshen–Kopelman algorithm to non-lattice environments" by A. Al-Futaisi and T.W. Patzek, Physica A **321** (2003) 665–678. Physica A **363**, 558–560 (2006)
29 Hoshen, J., Kopelman, R.: Percolation, cluster distribution. I. Cluster multiple labeling technique, critical concentration algorithm. Phys. Rev. B **14**, 3438–3445 (1976)
30 Argento, C., Bouvard, D.: Modeling the effective thermal conductivity of random packing of spheres through densification. International Journal of Heat and Mass Transfer **39**, 1343–1350 (1996)
31 Frohne, H., Moeller, F.: Moeller Grundlagen der Elektrotechnik, (22th edn.) Studium. Vieweg + Teubner, Wiesbaden (2011)
32 Jacob, B., Guennebaud, G.: Eigen. http://eigen.tuxfamily.org/
33 Carson, J.K., Lovatt, S.J., Tanner, D.J., et al.: Thermal conductivity bounds for isotropic, porous materials. International Journal of Heat and Mass Transfer **48**, 2150–2158 (2005)
34 Tobochnik, J., Lain, D., Wilson, G.: Randon-walk calculations of conductivity in continuum percolation. Physical Review A **41**, 3052–3058 (1990)
35 Bertei, A., Nicolella, C.: A comparative study and an extended theory of percolation for random packings of rigid spheres. Powder Technology **213**, 100–108 (2011)
36 Kuo, C.H., Gupta, P.K.: Rigidity and conductivity percolation threshold in particulate composites. Acta Metall. Mater. **43**, 397–403 (1995)
37 Dominko, R., Gaberšček, M., Drofenik, J., et al.: Influence of carbon black distribution on performance of oxide cathodes for Li ion batteries. Electrochimica Acta **48**, 3709–3716 (2003)
38 Dominko, R., Gaberšček, M., Drofenik, J., et al.: A novel coating technology for preparation of cathodes in Li-ion batteries. Electrochem. Solid-State Letters **4**, A187–A190 (2001)
39 Tarascon, J., Guyomard, D.: The "$Li_1 + xMn_2O_4$/C" rockingchair system: A review. Electrochimica Acta **38**, 1221–1231 (1993)
40 Hellweg, B.: Microstructural modeling of lithium battery electrodes. [Master Thesis], Massachusetts Institute of Technology, France (2000)
41 Martin, C., Bouvard, D.: Isostatic compaction of bimodal powder mixtures and composites. International Journal of Mechanical Sciences **46**, 907–927 (2004)